

Article

# Toughness Property Control by Nb and Mo Additions in High-Strength Quenched and Tempered Boron Steels

Irati Zurutuza <sup>1,2</sup>, Nerea Isasti <sup>1,2</sup>, Eric Detemple <sup>3</sup>, Volker Schwinn <sup>3</sup>, Hardy Mohrbacher <sup>4,5</sup> and Pello Uranga <sup>1,2,\*</sup>

<sup>1</sup> CEIT-Basque Research and Technology Alliance (BRTA), Materials and Manufacturing Division, 20018 Donostia/San Sebastián, Basque Country, Spain; izurutuza@ceit.es (I.Z.); nisasti@ceit.es (N.I.)

<sup>2</sup> Mechanical and Materials Engineering Department, Universidad de Navarra, Tecnun, 20018 Donostia/San Sebastián, Basque Country, Spain

<sup>3</sup> AG der Dillinger Hüttenwerke, 66763 Dillingen/Saar, Germany; Eric.Detemple@dillinger.biz (E.D.); Volker.Schwinn@dillinger.biz (V.S.)

<sup>4</sup> NiobelCon BV, 2970 Schilde, Belgium; hm@niobelcon.net

<sup>5</sup> Department of Materials Engineering (MTM), KU Leuven, 3001 Leuven, Belgium

\* Correspondence: puranga@ceit.es; Tel.: +34-943-212-800

**Citation:** Zurutuza, I.; Isasti, N.; Detemple, E.; Schwinn, V.; Mohrbacher, H.; Uranga, P. Toughness Property Control by Nb and Mo Additions in High-Strength Quenched and Tempered Boron Steels. *Metals* **2021**, *11*, 95. <https://doi.org/10.3390/met11010095>

Received: 21 December 2020

Accepted: 1 January 2021

Published: 5 January 2021

**Publisher's Note:** MDPI stays neutral with regard to jurisdictional claims in published maps and institutional affiliations.



**Copyright:** © 2021 by the authors. Licensee MDPI, Basel, Switzerland. This article is an open access article distributed under the terms and conditions of the Creative Commons Attribution (CC BY) license (<http://creativecommons.org/licenses/by/4.0/>).

**Abstract:** The synergetic effect on hardenability by combining boron with other microalloying elements (such as Nb, Mo and Nb + Mo) is widely known for high-strength medium carbon steels produced by direct quenching and subsequent tempering treatment. The improvement of mechanical properties could be reached through optimization of different mechanisms, such as solid solution hardening, unit size refinement, strain hardening, fine precipitation hardening and the effect of carbon in solid solution. The current study proposes a procedure for evaluating the contribution of different microstructural aspects on Charpy impact toughness. First, the effect that austenite conditioning has on low-temperature transformation unit sizes and microstructural homogeneity was analysed for the different microalloying element combinations. A detailed crystallographic characterization of the tempered martensite was carried out using electron backscattered diffraction (EBSD) in order to quantify the effect of unit size refinement and dislocation density. The impact of heterogeneity and presence of carbides was also evaluated. The existing equations for impact transition temperature (ITT50%) predictions were extended from ferrite-pearlite and bainitic microstructures to tempered martensite microstructures. The results show that microstructural refinement is most beneficial to strength and toughness while unit size heterogeneity has a particularly negative effect on ductile-to-brittle transition behaviour. By properly balancing alloy concept and processing, steel having a yield strength above 900 MPa and low impact transition temperature could be obtained by direct quenching and tempering.

**Keywords:** martensite; thermomechanical simulations; toughness properties; microalloying elements

## 1. Introduction

Quenching and tempering treatments are well established for achieving a favourable combination of strength and toughness properties for a wide range of applications. In quenched and tempered steels, packet size and particle distribution as well as brittle intergranular fracture modes by grain boundary segregation of impurities in ferrite (temper embrittlement) or precipitates in austenite are of importance. Anisotropy of toughness arises from banded structures especially when non-metallic inclusions such as MnS are stretched out [1].

Cooling installations in modern rolling mills allow for direct quenching from the rolling heat with the option of self-tempering or offline tempering. This approach is economically attractive. It has to be considered, however, that properties can be anisotropic, in this case due to austenite pancaking [2].

For ensuring full transformation into martensite of especially heavier gages under technically feasible cooling rates, hardenability-increasing alloying elements have to be used. The use of boron microalloying is common practice for achieving through hardening low- and medium-carbon manganese steels. However, boron must be segregated as the solute to the austenite grain boundary before quenching. Titanium microalloying protects the loss of solute boron as BN by forming more stable TiN. Furthermore, combined alloying of Nb and B as well as Mo and B has been described in the literature as enhancing boron's hardenability effect [2–6]. Both elements prevent boron from forming boron carbides ( $\text{Fe}_{23}(\text{C},\text{B})_6$ ) in the austenite grain boundaries that would reduce solute boron's effect of obstructing ferrite nucleation [7].

Usually, the tempering treatment softens the martensitic microstructure, thereby promoting an improvement of toughness and ductility [8,9]. However, the role of the different microstructural features must be taken into account in order to avoid brittle fracture behaviour [10]. Since the martensite substructure forms within the austenite grains prior to quenching [11], austenite conditioning has a significant impact on achieving an optimal balance of strength and toughness [12]. Several works analyse the role of the microstructure prior to austenitizing in terms of mechanical properties, and different ways of refining grain size have been proposed in the literature [13–15]. Thermomechanical treatment can affect the size and shape of the final martensite and the level of segregation at grain boundaries, favouring intergranular fracture. When microalloying elements are added, strong pancaking of austenite can be reached. A significant synergetic effect of combining Nb and B on recrystallization delay has been reported in several works [16]. The addition of Nb is widely used to delay the static recrystallization kinetics of austenite through two different mechanisms: solute drag and strain-induced precipitation [17]. This promotes the accumulation of deformation on the austenite prior to phase transformation, leading to microstructural refinement of the resulting microstructure and ensuring enhancement of both tensile and toughness properties [18].

In order to evaluate the effect of austenite conditioning in terms of microstructural homogeneity and toughness properties, austenitic structure characterization has to be performed. For equiaxed and polygonal austenite, analysis and quantification of the austenite grain size distribution usually relies on optical microscopy, yet for highly deformed austenitic structures, the austenite grain boundaries cannot be properly revealed by optical microscopy. Consequently, the use of the electron backscattered diffraction (EBSD) technique for reconstructing the prior austenite from the martensitic microstructure has become an essential tool for reliable quantitative characterization. In this respect, efforts on the development of several austenite reconstruction methods have been made recently [19–21].

Previous studies evaluated the effect of tempering treatment on directly quenched low-alloy ultrahigh-strength steels in terms of microstructure and mechanical properties [22,23]. Pallaspuo et al. [23] reported that low-impact transition temperatures at which 28 J of impact energy is reached (ITT<sub>28</sub>) can be achieved after direct quenching and that good toughness properties can be ensured without tempering treatment. However, they observed a reduction in yield strength and an improvement in ductility as well as toughness after tempering. They noticed a clear beneficial effect of microstructural homogeneity in martensite [23]. The presence of coarser effective grain sizes reflects the longer tailing out of unit size distributions curves. These result in the deterioration of toughness properties. The improvement of toughness observed for the direct quenched as compared to the reheated and quenched states is attributed to the formation of more homogeneous martensitic microstructures with a lower fraction of coarse grains [23]. The positive effect of austenite pancaking on martensite homogeneity has also been reported by

Saastamoinen et al. [24]. In addition, they concluded that the effective grain size at 90% cut-off in the cumulative grain size distribution is the key criterion controlling toughness properties for both the Direct Quenching (DQ) and DQ+tempering (DQ+T) processing strategies. Regarding the effect of boron in terms of tensile/toughness properties, Hannula et al. [12] studied the influence of adding boron to a low-carbon Nb microalloyed martensitic steel. It was demonstrated that removing boron significantly improved the toughness properties due to the formation of a finer and more homogeneous martensitic microstructure in the B-free steel. In another work, Hannula et al. [25] analysed the impact of adding Mo and Nb on the martensitic microstructure and mechanical properties of laboratory-rolled DQ and DQ+T plates. They observed that the addition of Mo and Nb improves the strength considerably (0.25 Mo–Nb) via an increased dislocation density and fine precipitation hardening. However, 0.25 Mo–Nb steel shows worse toughness properties compared to 0.25 Mo steel due to intense precipitation hardening in the Nb-grade. Even though upgrading tensile properties could be reached through optimization of different strengthening mechanisms, toughness properties could be impaired. In this context, the exact interaction between toughness properties and the different microstructural features has to be better understood. Effort has been made in that respect regarding toughness properties in ferritic and non-polygonal bainitic microstructures [26–29].

Several relationships have been proposed in the literature for quantitatively predicting the impact transition temperatures [28–31]. Most of the proposed approaches consider the impact of solid solution, pearlite fraction, dislocation density and fine precipitation (both represented by the  $\Delta\sigma_y$  term), carbide thickness ( $t$ ) and unit size refinement. The transition temperature can be represented by different definitions, one of them being the fracture appearance transition temperature (ITT50%). Most approaches were derived from analysing low-carbon ferrite-pearlite steels. These equations account for microstructural grain size heterogeneities. Several works suggested that a parameter accounting for the presence of coarse grains and microstructural heterogeneity is required for accurately predicting the ductile-to-brittle transition temperature [32,33]. In that sense, Larzabal et al. [34] proposed a relationship (Equation (1)) to predict ITT50% for low-carbon Nb, NbMo and TiMo microalloyed steels, thereby taking into account the effect of microstructural heterogeneity and the presence of hard secondary phases such as pearlite and Martensite-austenite (MA) islands. This relationship is applicable to ferritic-pearlitic and bainitic microstructures [34].

$$\begin{aligned} ITT50\%(^{\circ}C) = & -11Mn + 42Si + 700(N_{free})^{0.5} + 15(pct\ Pearlite + pct\ MA)^{\frac{1}{3}} + 0.26\Delta\sigma_y - 14(D_{15^{\circ}})^{-0.5} \\ & + 63\left(\frac{D_{20\%}}{D_{15^{\circ}}}\right)^{0.5} + 18(DMA)^{0.5} - 42 \end{aligned} \quad (1)$$

where  $D_{15^{\circ}}$  is the high angle boundary unit size,  $D_{20\%}$  is the cut-off unit size at the 80% area fraction in a grain size distribution and DMA is the average MA island size.

The present study aims to modify and extend this relationship for use in martensitic steels. In this context, the relationship between microstructure and toughness properties is analysed in four different boron microalloyed carbon–manganese steels after direct quenching and tempering treatment. The strength properties of the same steels have been recently published [35]. A model predicting the yield strength has been proposed and validated for both the quenched and tempered martensitic conditions incorporating the interaction between the quenched microstructure, the tempering treatment and the addition of microalloying elements [35]. Specific effects related to alloying of niobium and molybdenum have been revealed as well. For understanding the toughness properties, Charpy tests are performed with the same alloys in direct quenched and tempered conditions. Based on elaborate microstructural characterization, a modified relationship for predicting ITT50% is defined and validated. This platform allows for the definition of optimized alloy concepts and processing strategies for obtaining superior strength and toughness properties in tempered martensitic steels.

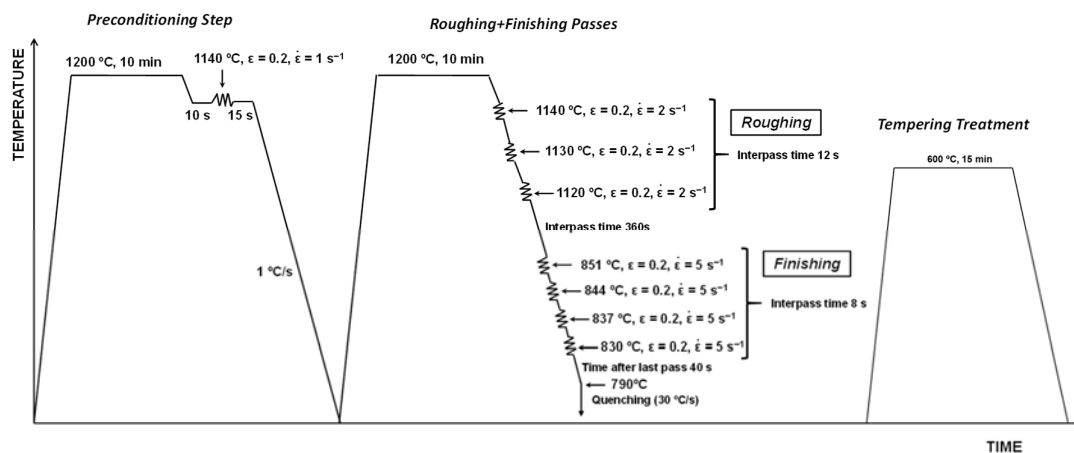
## 2. Materials and Methods

Table 1 shows the chemical composition of the selected medium carbon steels with 0.16% of C and 20 ppm of boron. Besides a CMnB steel, three different microalloyed steels were also studied, microalloyed with Nb, Mo and NbMo. The Nb level is 0.026%, and Mo content is about 0.5%.

**Table 1.** Chemical composition of the studied steels (weight percent).

Steel	C	Si	Mn	Mo	Nb	B
CMnB	0.15	0.32	1.05	-	-	0.0022
CMnNbB	0.16	0.29	1.05	-	0.026	0.0019
CMnMoB	0.16	0.28	1.07	0.5	-	0.0022
CMnNbMoB	0.16	0.31	1.07	0.5	0.026	0.0018

Plane strain compression tests were carried out in order to simulate the plate hot rolling process followed by direct quenching and subsequent tempering treatments. Deformation by plane strain compression was carried out in a servo-hydraulic machine equipped with an induction furnace for reheating. After this stage, the specimen was automatically transferred to a resistance furnace that was set at the deformation temperature and inside which the tools were kept hot. The specimen temperature was continuously monitored by an inserted thermocouple. Rectangular samples 60 mm long, 30 mm wide and 22 mm thick were used with a tool width of 15 mm. The cycle started with a preconditioning step, with the purpose of ensuring the refinement of the as-cast austenitic structure and minimizing the presence of coarse austenite grains at the reheating temperature (see the thermomechanical schedule in Figure 1). Then, the plate hot rolling simulation was carried out based on reheating at 1200 °C for 10 min followed by three roughing deformation passes ( $\epsilon = 0.2$  at  $2 \text{ s}^{-1}$  and an interpass time of 3 s) at decreasing temperature in the interval between 1140 and 1120 °C. Subsequently, after holding for 360 s, 4 finishing passes were applied (strain of 0.2 at  $5 \text{ s}^{-1}$  with an interpass time of 8 s) in the temperature range between 851 and 830 °C. Finally, accelerated cooling was applied until room temperature (cooling rate of about  $30 \text{ °C/s}$  above  $300 \text{ °C}$  and below a cooling rate of approximately  $10 \text{ °C/s}$ ). Afterwards, a tempering treatment was carried out at  $600 \text{ °C}$  for 15 min. Full details of the thermomechanical schedule can be found in Reference [35].



**Figure 1.** Schematics of the applied plane strain compression cycle.

Plane compression samples show that heterogeneous strain distribution through thickness was associated with the geometry and friction of the sample/tool [36]. Therefore,

the specimens used for the microstructural characterization and Charpy tests were machined from the centre of the plane strain compression samples, with the purpose of minimizing strain gradients along the section of the plane strain compression samples.

Different characterization techniques were employed for microstructural characterization, such as optical microscopy (OM, LEICA DM15000 M, Leica microsystems) and field-emission gun scanning electron microscopy (FEGSEM, JEOL JSM-7100F). Besides analysing the martensitic microstructure after etching with Nital 2%, the austenitic structures were also characterized after etching in a solution of saturated picric acid and HCl after polishing. For crystallographic unit sizes, measurements of the martensitic microstructure electron backscattered diffraction (EBSD) technique were employed. Additionally, EBSD data were used for reconstruction of the prior austenite grain orientation, and the approach described in [19,20] was applied. EBSD sample preparation consisted of a conventional polishing route, using diamond liquids down to 1  $\mu\text{m}$  and final polishing with colloidal silica. EBSD was performed on the equipment with a camera NORDLYS II with an acquisition program and data analysis, OXFORD HKL CHANNEL 5 PREMIUM coupled to the JEOL JSM-7100 F (FEG-SEM). The selected step size and scanned area varied depending on the required resolution. A scan step size of 0.2  $\mu\text{m}$  and a total scanned area of  $140 \times 140 \mu\text{m}^2$  were defined for unit size quantification. For reconstructing the austenite prior to transformation, higher scanned area of  $300 \times 300 \mu\text{m}^2$  was used and a step size of 0.5  $\mu\text{m}$  was defined. Two different crystallographic unit sizes were defined based on low- and high-angle boundaries. Low-angle units were defined for grain boundary misorientation between 2 and  $15^\circ$ , whereas high-angle unit sizes were set for a grain boundary misorientation higher than  $15^\circ$ .

Regarding toughness property evaluation, Charpy sub-size specimens (approximately  $4 \times 10 \times 55 \text{ mm}^3$ ) were machined from the central part of the plane strain compression samples, and Charpy tests were carried out within a  $-120$  to  $40^\circ\text{C}$  test temperature range (Tinius Olsen Model Impact 104 pendulum impact tester with maximum capacity of 410J). The proportionality rule shown in Equation (2) can be assumed for these Charpy specimen thicknesses [28].

$$K_{v10} = \frac{10}{B} K_{vB} \quad (2)$$

where  $K_{v10}$  and  $K_{vB}$  are the absorbed impact energy for 10 mm and B sample thickness, respectively. For determining the impact transition curves, the modified hyperbolic tangent fitting algorithm suggested by Wallin was considered [37].

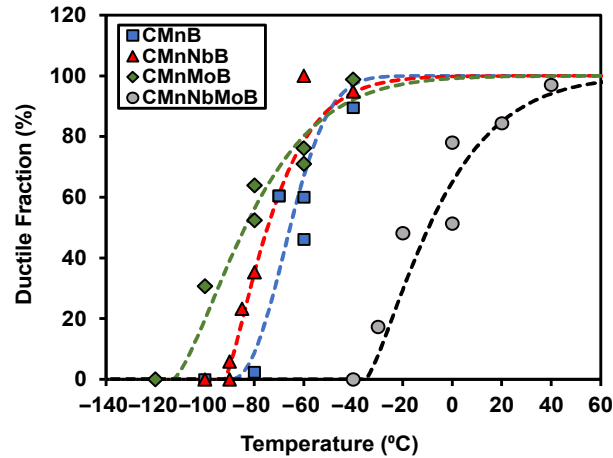
### 3. Results and Discussion

#### 3.1. Mechanical Behaviour

In Table 2, upper-shelf energies (US) as well as the transition temperatures for an impact energy value of 27 J (ITT27 J) and the temperature at which the sample shows a 50% ductile–brittle appearance (ITT50%) are shown. Yield strength and tensile strength values previously reported in [35] are included. Figure 2 shows the comparison between the impact transition curves measured in each chemical composition (ductile fraction is plotted as a function of test temperature). Slightly better toughness properties are observed in CMnNbB and CMnMoB steels compared to the CMnB grade one. ITT50% values of  $-66$ ,  $-75$  and  $-84^\circ\text{C}$  were quantified for the CMnB, CMnNbB and CMnMoB grades, respectively. Conversely, when Nb and Mo were added simultaneously, the impact transition curve shifted to higher temperatures, showing worse toughness properties (an ITT50% of  $-10^\circ\text{C}$  was measured in NbMo microalloyed steel).

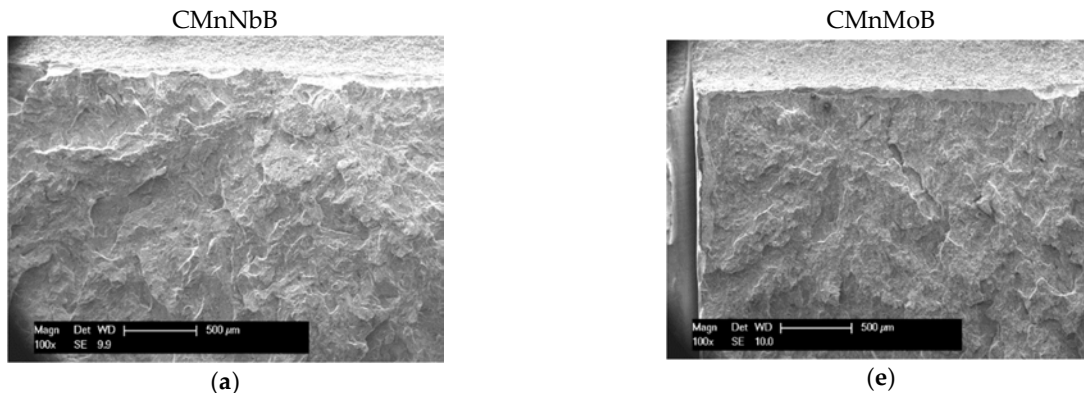
**Table 2.** US (Upper-Shelf Energy), ITT27J, ITT50%, yield strength and tensile strength values measured from Charpy and tensile tests.

Steel	US (J)	ITT 27 J (°C)	ITT 50% (°C)	Yield Strength (MPa)	Tensile Strength (MPa)
CMnB	108	-63	-66	617	700
CMnNbB	112	-59	-75	757	818
CMnMoB	97	-80	-84	943	991
CMnNbMoB	82	-1	-10	977	1034



**Figure 2.** Effect of the addition of microalloying elements on toughness properties (ductile fraction as a function of test temperature).

Detailed fractographic examination was performed on the tested Charpy samples (fracture surfaces were analysed) with the aim of evaluating possible cleavage crack-initiation sites and microstructural features in their vicinity. In Figure 3, cleavage initiation sites are shown at different magnifications for CMnNbB and CMnMoB steels (test temperature of  $-100^{\circ}\text{C}$  and  $-120^{\circ}\text{C}$ , respectively). In the martensitic microstructures, crack initiators are not easy to detect. However, differences in the facet sizes are observed depending on the chemistry. Coarser facets are noticed in the CMnNbB grade steel (see Figure 3a) whereas CMnMoB shows the finest facets (see Figure 3c). Additionally, fracture surfaces were analysed after Nital 2% etching in order to better distinguish the microstructural features controlling the fracture. In both steels, some inclusions, such as coarse Ti nitride particles, were identified in the crack-initiation regions, as shown in Figure 3b,d.



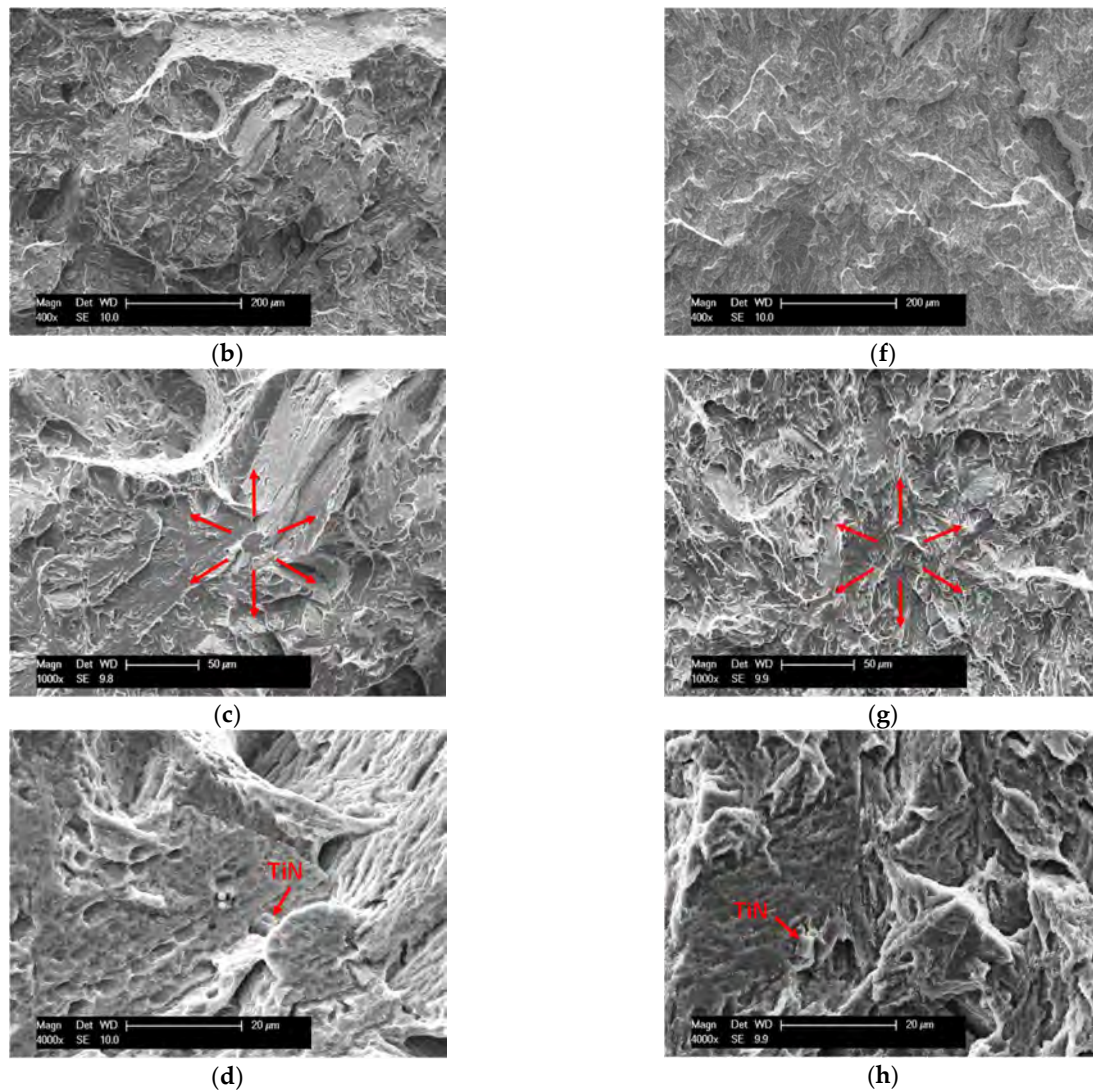


**Figure 3.** Fracture surfaces at different magnifications showing the crack-initiation site: (a–d) CMnNbB (test temperature of  $-100\text{ }^{\circ}\text{C}$ ) and (e–h) CMnMoB (test temperature of  $-120\text{ }^{\circ}\text{C}$ ).

### 3.2. Microstructural Characterization

#### 3.2.1. Analysis of the Prior Austenitic Structure

Optical micrographs illustrating the parent austenite grain structures are shown in Figure 4. A completely different austenite morphology is noticed depending on the alloy composition. In CMnB steel, equiaxed austenite grains are observed, as shown in Figure 4a. In the Nb-added alloy, a combination of pancaked and very small equiaxed grains is observed. The small grains originate from dynamic recrystallization (DRX) due to the accumulated strain reflected on the high degree of pancaking. For Mo-containing grades, a strong accumulation of deformation on austenite is reflected by a fully pancaked microstructure (see Figure 4c,d, for CMnMoB and CMnNbMoB, respectively).

The delay that molybdenum and niobium exert on dynamic recrystallization kinetics is associated with two different phenomena. On the one hand, the solute drag of both Mo and Nb impedes the mobility of high-angle boundaries [38–40]. On the other hand, dynamic recrystallization could be affected by the impact of Mo on the Nb carbonitride precipitation. It is reported that molybdenum reduces the diffusivity of carbon in austenite [41], lowering the available C and consequently reducing Nb(C,N) formation. Therefore,

a higher content of Nb remains in solution, impeding grain boundary mobility. Nb in solid solution has a stronger effect than Nb-based precipitates in hindering the movement of grain boundaries during DRX [42].

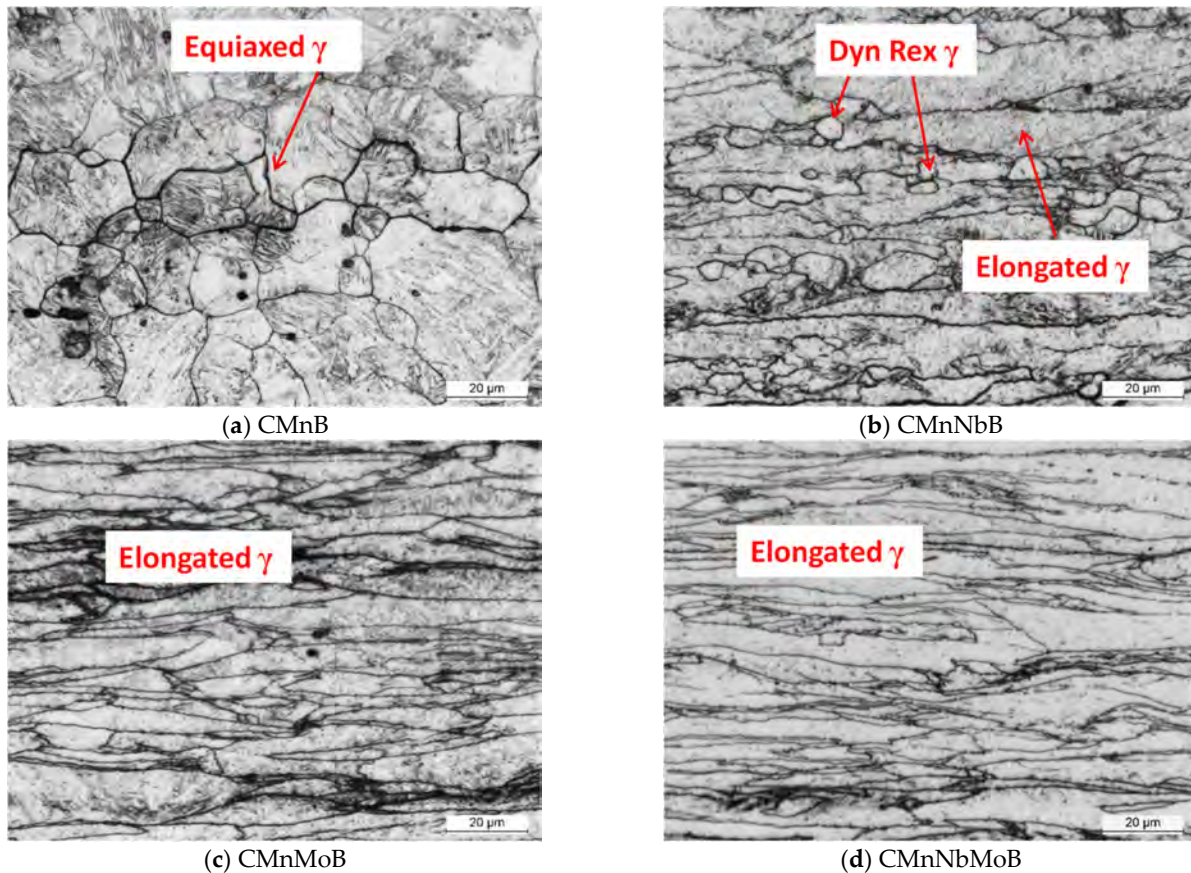


**Figure 4.** Optical micrographs of the austenite structure after quenching corresponding to (a) CMnB, (b) CMnNbB, (c) CMnMoB and (d) CMnNbMoB steels (picric acid etching is used).

For highly deformed austenitic structures, the austenite grain boundaries are not properly revealed by chemical etching, and therefore, characterization of the austenitic structure by optical microscopy becomes more complex. In this respect, the use of the EBSD technique for reconstruction of the prior austenite has become an essential tool for characterizing and quantifying the austenitic structure from the orientation relationships between the parent austenite and final martensite [19,20]. Figure 5 shows the results for the reconstruction technique applied to CMnB and CMnNbMoB steels. The applied methodology starts by performing an EBSD scan in a selected area (see Figure 5a,e for CMnB and CMnNbMoB steels, respectively). EBSD maps and optical micrographs are aligned with the compression deformation direction parallel to the vertical axis. From the martensitic microstructures, the parent austenite grain structure prior to transformation is calculated. In order to validate the austenite reconstruction procedure, the samples were subsequently etched by picric acid and analysed by optical microscopy in the same region where the EBSD scan was performed, as illustrated in Figure 5c,g. Additionally, the austenite grains were manually drawn in each case with the purpose of quantifying the austenite grain size distribution in the same area by OM. Figure 5d,h presents the comparison between austenite grain size distributions measured by the EBSD technique (considering a tolerance angle of  $10^\circ$ , as previously proposed in [20]) and by optical microscopy (considering equivalent diameter method). Analysing Figure 5d,h confirms that quite similar austenite size distributions are achieved by both techniques (EBSD and OM).

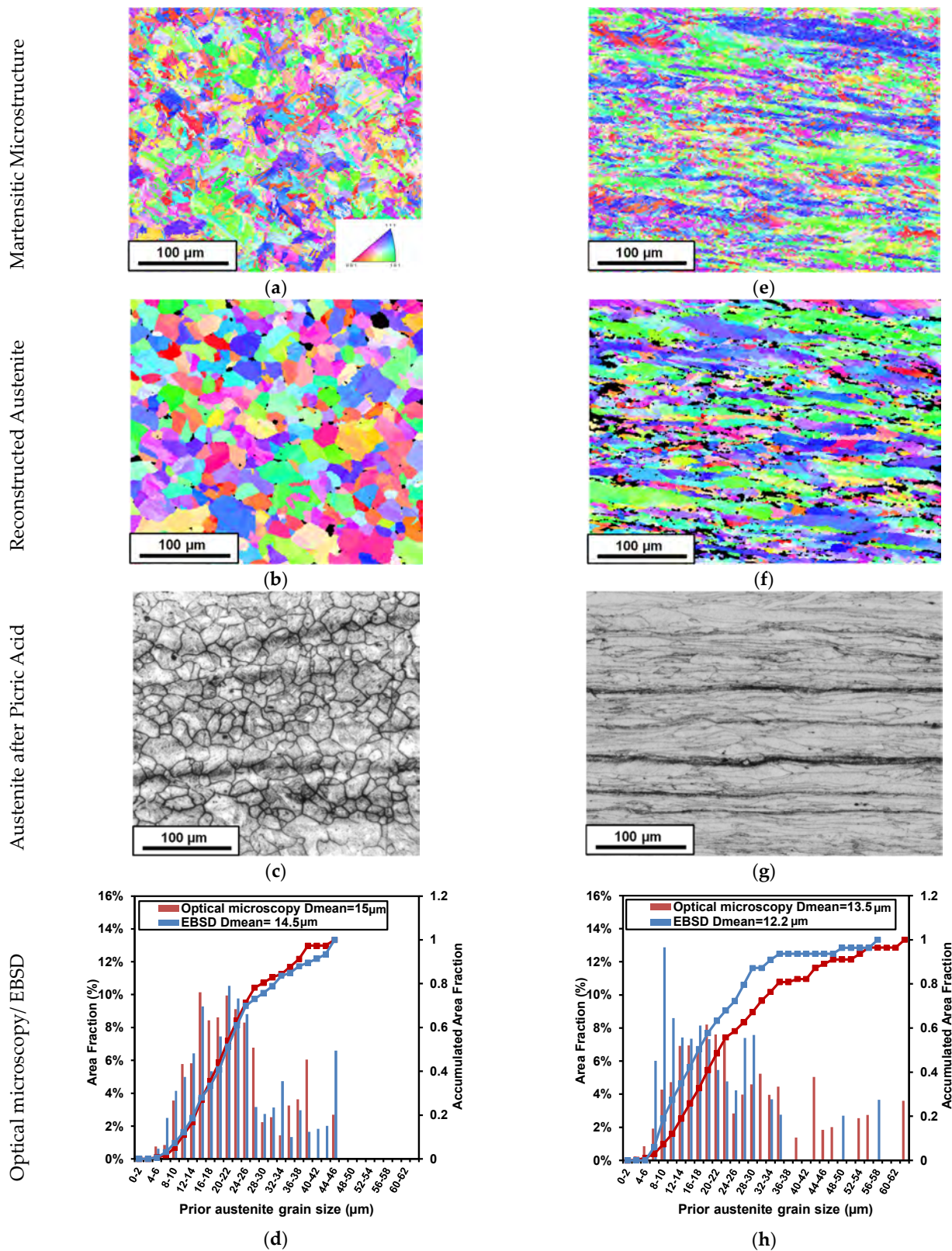


**Figure 5.** (a,e) Martensitic microstructure, (b,f) reconstructed austenite by electron backscattered diffraction (EBSD), (c,g) optical images corresponding to austenite obtained after picric acid, (d,h) austenite size distributions measured by optical microscopy and EBSD technique for (a–d) CMnB and (e–h) CMnNbMoB steels (Applied strain direction, equivalent to rolling direction (RD), is considered for Inverse Pole Figure (IPF) representation).

### 3.2.2. Quantification of Mean unit Sizes and Microstructural Homogeneity

High-resolution EBSD scans were also carried out to measure martensite unit sizes. High-angle boundaries act as effective obstacles to cleavage fracture, and therefore, the effective unit size affecting toughness properties was defined by a threshold of  $15^\circ$  ( $D15^\circ$ ). Figure 6a,b shows the grain boundary maps corresponding to Nb and NbMo microalloyed steels, respectively. Low-angle boundaries, between  $2^\circ$  and  $15^\circ$ , are shown in red, whereas high-angle boundaries ( $>15^\circ$ ) are drawn in black. In both steel grades, complex microstructures as well as very fine unit sizes can be distinguished. When Mo is added to Nb microalloyed steel, an increase in the low-angle boundaries is apparent and the martensitic matrix presents a more pronounced substructure (see Figure 6b). For evaluating the density of different boundary types, the grain boundary length per unit area was calculated [43]. Concerning low-angle boundaries between  $2^\circ$  and  $15^\circ$ , grain boundary length values per unit area of 0.98, 1.55, 1.79 and  $1.98 \mu\text{m}^{-1}$  are measured for CMnB, CMnNbB, CMnMoB and CMnNbMoB steels, respectively. The low-angle boundary density increases with the addition of microalloying elements, reaching the highest density in the NbMo-microalloyed grade.

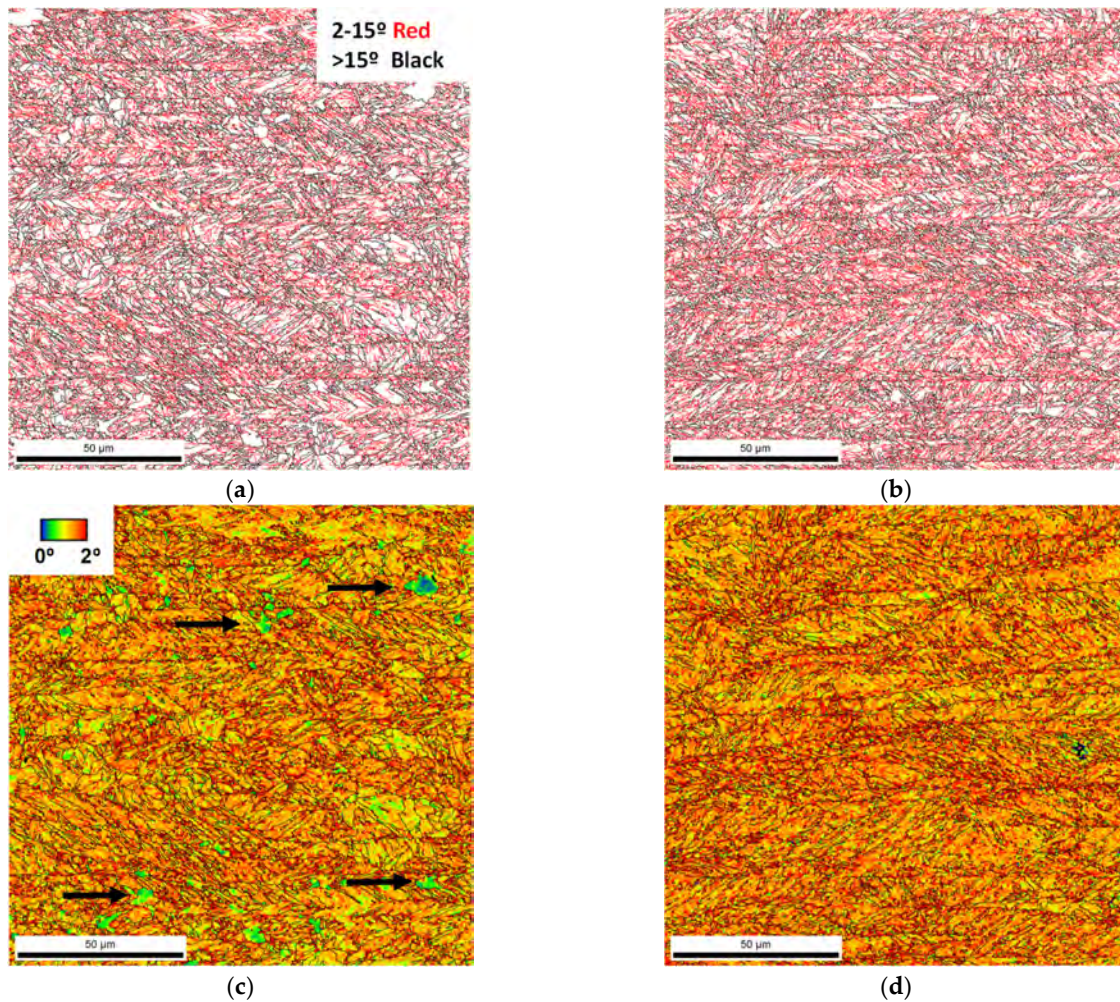
Additionally, the dislocation density is evaluated from Kernel Average Misorientation (KAM) maps [34,44]. For the calculation of KAM maps, misorientation lower than  $2^\circ$  is assumed and the third neighbour is selected. Figure 6c,d shows the Kernel maps corresponding to Nb- and NbMo-microalloyed steels, respectively. For the CMnNbMo steel (see Figure 6d), the KAM map is mainly coloured by yellow-orange, reflecting the presence of a highly dislocated tempered martensite. However, in the Nb-microalloyed steel (see Figure 6c), in addition to regions represented in yellow-orange, some grains coloured by blue-green can be clearly distinguished (see black arrows in Figure 6c), showing the presence of grains with lower dislocation density in the martensitic matrix. This is attributed to the formation of non-polygonal ferritic islands within the martensitic microstructure of the CMnNbB steel. Furthermore, these ferritic grains are characterized by the lack of substructure, as can be clearly observed in the grain boundary map shown in Figure 6a.

Within the softer ferritic phase, low angle boundaries (drawn in red) are absent (see Figure 6a). The presence of non-polygonal ferritic islands inside a martensitic matrix cannot be due to a lack of a cooling rate. It rather indicates that the obstruction of ferrite nucleation by solute boron was locally not effective. Since solute boron must be segregated to the austenite grain boundary for deploying this effect, it is reasonable to assume that an insufficient amount of boron was present in part of the grain austenite boundaries. It also appears that, in the CMnNbB steel, where this phenomenon is observed, the very small equiaxed dynamically recrystallized austenite islands (Figure 4b) coincide with these ferritic islands revealed in Figure 6c. It is possible that, at the instant of dynamic recrystallization, insufficient solute boron was left in the austenite matrix for segregation to these newly formed austenite grain boundaries, rendering a higher density of nucleation sites for ferrite formation.

Distribution diagrams of high-angle boundary unit sizes are plotted in Figure 6e for the different alloys. The measurements suggest that the addition of both Nb and Mo is beneficial as these elements promote the formation of finer unit sizes. However, when Nb and Mo are added in combination, a substantial fraction of coarser unit sizes appears in the distribution diagram, indicating the presence of mixed prior austenite grain sizes. This inhomogeneous austenite grain structure must originate from austenite conditioning. Principally, the two-stage deformation schedule applied in this study refines austenite grains by multiple recrystallizations during the first stage at higher temperature. The second deformation stage at lower temperature pancakes the formerly equiaxed austenite grains. Accordingly, size inhomogeneities can occur when an inhomogeneous grain structure is produced during the first deformation stage, for instance, by partial recrystalliza-

tion provoking individual grains growing to larger sizes. Oppositely, dynamic recrystallization during severe pancaking in the second rolling stage can produce very fine austenite grains, which were observed in the CMnNbB steel (Figure 4b).

In Mo- and NbMo-microalloyed steels, austenite exhibits a pronounced pancake morphology prior to quenching caused by solute drag of Mo atoms and particle pinning related to Nb-based precipitates. A finer austenite thickness leads to finer effective grain size, resulting in improved tensile and toughness properties. By applying direct quenching after austenite conditioning, the martensite packet size is directly related to the austenite pancake thickness [45]. In Table 3, the  $S_v$  parameter related to the austenite boundary area per unit volume as well as the average austenite pancake thickness measured by optical microscopy are summarized. In addition, mean unit sizes quantified by EBSD technique are shown. The lowest  $S_v$  value is found for CMnB steel, and the coarsest austenite thickness is obtained. When Nb and/or Mo are added, the  $S_v$  parameter increases significantly, leading to a clear reduction of the austenite thickness. For CMnMoB grade steel, the  $S_v$  parameter reaches a maximum and the austenite thickness is the lowest. The strong accumulation of austenite deformation prior to transformation induces considerable refinement of the resulting martensitic microstructure. The lowest mean unit sizes ( $D_{2^\circ}$  and  $D_{15^\circ}$  values) are measured when Nb and Mo are added in combination, despite the smaller  $S_v$  parameter and larger austenite thickness compared to CMnMoB grade steel.



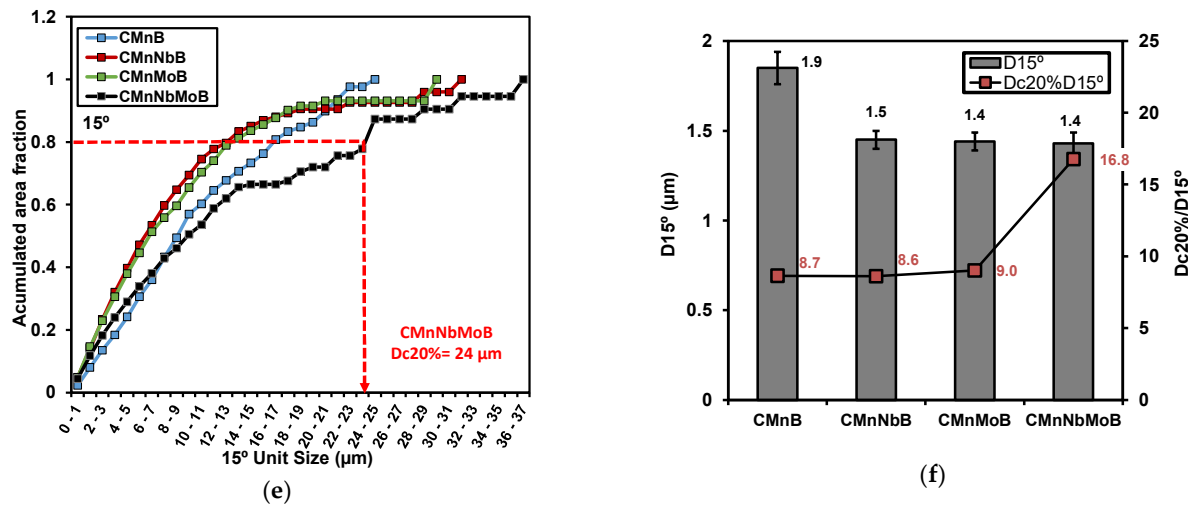


**Figure 6.** (a,b) Grain boundary maps and (c,d) Kernel maps corresponding to (a,c) Nb and (b,d) NbMo grades, (e) comparison between the unit size distributions taking into account 15° misorientation criteria and (f) D15° and Dc20%/D15° values measured for each steel grade.

**Table 3.** Measured Sv parameter (grain boundary area per unit volume) and average austenite thickness for the different alloys: mean unit sizes were quantified by EBSD considering low- and high-angle misorientation criteria.

Steel	Sv ( $\mu\text{m}^{-1}$ )	Austenite Thickness ( $\mu\text{m}$ )	D2° ( $\mu\text{m}$ )	D15° ( $\mu\text{m}$ )
CMnB	0.13	12.9 ± 0.8	1.26 ± 0.03	1.85 ± 0.1
CMnNbB	0.24	5.5 ± 0.2	0.92 ± 0.01	1.45 ± 0.05
CMnMoB	0.30	4.9 ± 0.2	0.86 ± 0.1	1.44 ± 0.05
CMnNbMoB	0.23	6.9 ± 0.4	0.85 ± 0.01	1.43 ± 0.06

In Figure 6f, the mean unit sizes measured for each steel grade are plotted together, assuming high-angle misorientation criteria (higher than 15°). The heterogeneity of the microstructure is measured by the Dc20% parameter [34], which is considered a useful criterion for defining the tail-out length of a size distribution curve. It corresponds to the cut-off unit size at the 80% area fraction in a grain size distribution, as indicated in Figure 6e. The ratio of Dc20%/D15° shown in Figure 6f increases considerably for the CMnNbMoB, indicating the presence of a more heterogeneous microstructure. The Dc20%/D15° ratios for the other alloys are nearly identical and approximately half of that found in the CMnNbMoB steel. From the data, it can be concluded that the inhomogeneity must have been generated during the first deformation stage. Djahazi et al. [46] demonstrated that the addition of boron to a Nb-microalloyed steel accelerates the precipitation of Nb(C,N) and induces it to occur at higher temperatures. Additionally, boron and molybdenum segregating to grain boundaries and dislocations can retard recrystallization after deformation. It is thus possible that particularly the combined alloying of niobium, molybdenum and boron already impedes recrystallization at rather high deformation temperatures [47], resulting in individual unrecrystallized austenite grains growing in size.

### 3.2.3. Quantification of Carbide Size and Area Fraction

Tempering treatment causes modification of the quenched martensite, leading to the formation of carbides. In Figure 7, FEGSEM images at high magnifications of the different steel alloys are presented. Depending on the chemistry, the impact of tempering differs considerably, and slightly coarser carbides are identified in CMnB grade steels (Figure 7a) and finer carbides are detected in the steels containing Mo (Figure 7c,d). In the tempered

martensite, different types of carbides can be clearly distinguished [8]. Part of these carbides precipitates within the laths (at lath boundaries or other low-angle boundaries), while the other carbide fractions precipitate at high-angle boundaries, such as the prior austenite grain boundaries as well as martensite packet or block boundaries (Figure 7c). The latter carbides are generally coarser than those precipitating within the laths.

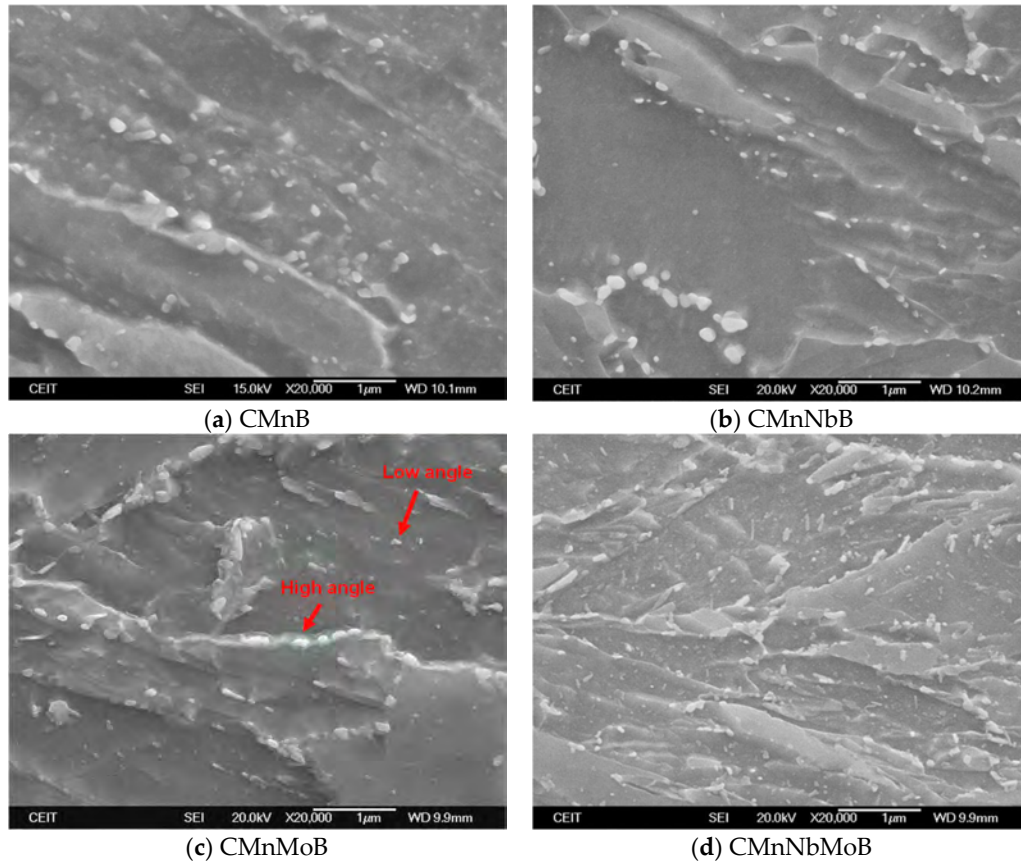


**Figure 7.** Field-emission gun scanning electron microscopy (FEGSEM) micrographs corresponding to (a) CMnB, (b) CMnNbB, (c) CMnMoB and (d) CMnNbMoB steels.

The carbide size and area fraction were evaluated for all alloys, taking into account both types of carbides located at low-angle (LAB) and high-angle (HAB) boundaries. The carbide size distributions shown in Figure 8 confirm that, for all alloys, the carbides located at high-angle boundaries are coarser than the carbides located at low-angle boundaries. Generally, coarser carbide size distributions are found in CMnB and CMnNbB steel as compared to the two alloys containing Mo. The carbides located at low-angle boundaries in the Mo-alloyed steels have approximately half the size compared to those in Mo-free steels. Furthermore, a higher area fraction of carbides is measured in the Mo-containing grades. Therefore, it can be concluded that Mo alloying promotes refinement of carbides and an increase in volume fraction. It was outlined in a previous paper [35] on the same steels that molybdenum participates in carbides of the MC, M<sub>2</sub>C, M<sub>6</sub>C and M<sub>23</sub>C<sub>6</sub> types while Nb forms only MC-type carbides.

As both carbide populations, i.e., at high- and low-angle boundaries, are considered to have similar detrimental effects on toughness, only the total carbide population is taken into account for further interpretation. The characteristics of the total carbide population in the four alloys are summarized in Table 4. In addition to carbide size refinement caused by the addition of Mo and NbMo, a clear increment of carbide density is detected when

molybdenum is added. A synergy between Mo and Nb with regard to carbide area fraction is apparent.

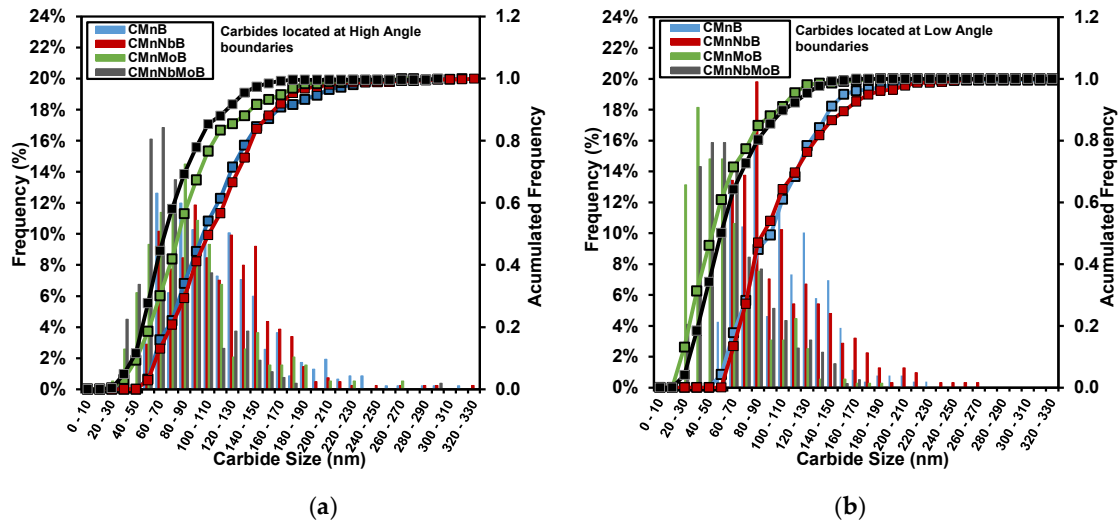


**Figure 8.** Comparison between carbide size distributions corresponding to the different steels and considering both grain boundaries: (a) carbides located at high-angle boundaries and (b) carbides located at low-angle boundaries.

**Table 4.** Measured mean carbide sizes and carbide densities considering total carbide population (sum of high-angle and low-angle boundaries).

Steel	Carbide Size (nm) (Total Carbide Population)	Area Fraction (%) (Total Carbide Population)
CMnB	110.1 ± 3	0.54
CMnNbB	111.3 ± 2.9	0.60
CMnMoB	70.6 ± 3	1.46
CMnNbMoB	72.3 ± 2.4	1.72

### 3.2.4. Additional Contributions to Toughness

Besides the influence of effective unit size and carbide population and among the different microstructural aspects, the presence of secondary hard phases, hardening due to dislocation density and fine precipitation, as well as the strengthening associated with carbon in solid solution have impacts on toughness. In the following paragraphs, a more detailed study of each of these influencing factors will be considered.

#### (1) Presence of hard secondary phases

Concerning the differences in the final microstructures depending on alloy composition, the presence of non-polygonal ferrite is also observed when Nb is added. In the FEGSEM image shown in Figure 9a, ferritic regions can be clearly distinguished in the martensitic matrix. Within the observed softer phase, martensite-austenite (MA) islands are also detected, as shown in Figure 9a. It is commonly known that hard secondary phases, such as MA islands, can have a detrimental effect on toughness properties [48]. Accordingly, the quantification of MA size and fraction is required [49].

In the current work, MA island volume fraction as well as MA mean size ( $D_{MA}$ ) were determined by quantitative metallography on optical micrographs (using the mean equivalent diameter method) after colour etching in LePera reagent [50]. In Figure 9b, an optical micrograph after colour etching is shown. Martensitic matrix and regions composed of non-polygonal ferrite are in brown, whereas MA islands can be distinguished in white. A low fraction of MA islands is measured in CMnNbB steel, approximately 0.04%, and mean MA size is about 0.79  $\mu\text{m}$ . In the other alloys, an MA microconstituent has not been detected. The formation of these MA islands must be a consequence of the ferrite growth

explaining the close proximity of these phases. Since the carbon solubility in ferrite is very small, carbon partitions with growth of the ferrite phase are enriched in a residual austenite phase. The relative sizes of these microstructural features allow for the estimation that the carbon content in the MA phase should be indeed high enough ( $>0.8\%$ ) for stabilizing austenite at ambient temperature after quenching. It has to be pointed out, however, that these MA islands should also decompose by the tempering treatment.

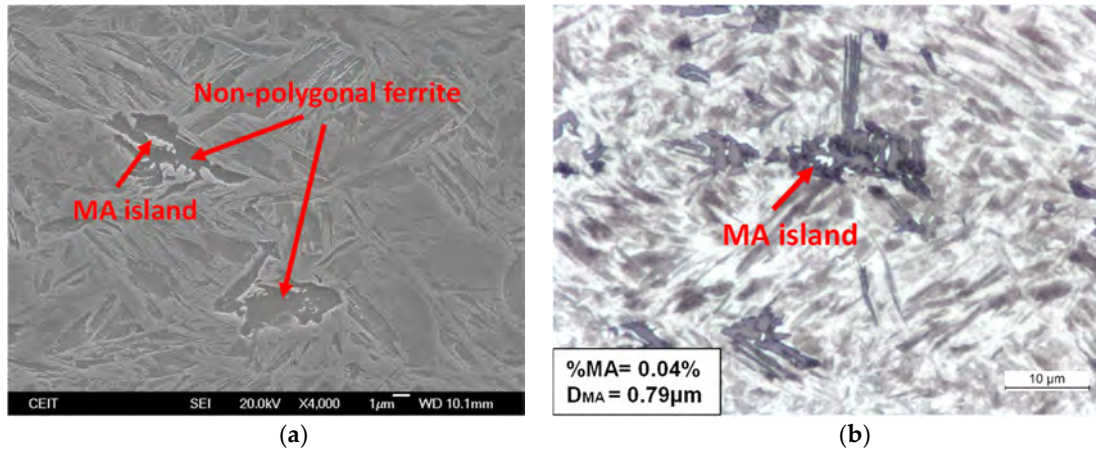


**Figure 9.** Presence of non-polygonal ferrite within martensitic matrix and martensite-austenite (MA) islands in CMnNbB steel: (a) FEGSEM micrograph and (b) optical image after LePera colour etching.

- (2) Hardening due to dislocation density, fine precipitation and carbon in solid solution

Modification of mechanical properties caused by dislocation density and fine precipitation in ferrite-pearlite and bainitic microstructures is represented by a  $\Delta\sigma_y$  term ( $\Delta\sigma_y = \Delta\sigma_d + \Delta\sigma_{ppt}$ ). The effect of  $\Delta\sigma_y$  on toughness can vary depending on the source. An effect of  $0.45\text{ }^\circ\text{C}\cdot\text{MPa}^{-1}$  is observed by Pickering [51] for a ferritic phase, while a value of  $0.26\text{ }^\circ\text{C}\cdot\text{MPa}^{-1}$  is observed for the bainitic constituent. In a recently published work, the contribution of  $\Delta\sigma_y$  to ITT50% has also been determined to be  $0.26\text{ }^\circ\text{C}\cdot\text{MPa}^{-1}$  [34].

In the analysis published in Reference [35], the hardening caused by solute carbon and fine precipitation is included in the unaccounted strength term. Figure 10 shows their contribution to yield strength for the different chemistries. Dislocation strengthening ( $\sigma_d$ ) slightly increases when microalloying elements are added, increasing from 112 to 121 MPa for CMnB and Mo-microalloyed steel, respectively. The contribution related to unaccounted strength ( $\sigma_{us}$ ) is nearly negligible for CMn and Nb steels, whilst for Mo containing grades, the impact of this contribution is considerably higher (185 and 229 MPa, for CMnMoB and CMnNbMoB, respectively). This larger yield strength could be attributed to the formation of ultrafine Mo-based precipitates during the tempering treatment that was also observed by TEM analysis. The synergy between Mo and Nb further enhances this precipitation strengthening effect.

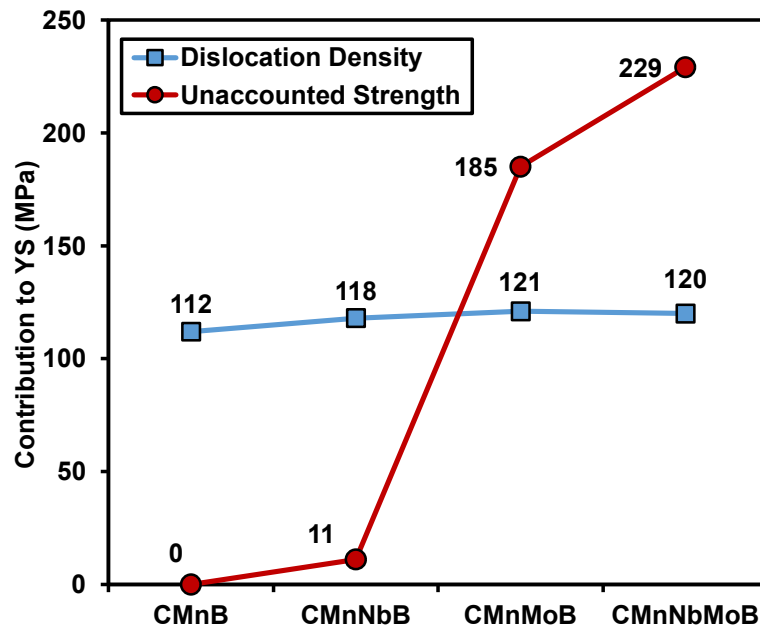


Figure 10. Dislocation density and unaccounted strength values corresponding to all steel grades.

### 3.3. Quantitative Relationship between Microstructure and Transition Temperature

A recent study on low carbon Nb-, NbMo- and TiMo-microalloyed steels [34] proposed an equation for predicting the impact transition temperature (ITT50%), taking into account the effect of microstructural heterogeneity and the presence of hard secondary phases such as MA islands (Equation (1)). In addition to the effect of chemical composition, the positive effect of refining cleavage unit size, the detrimental effect of heterogeneity, and MA size and fraction were taken into account. For considering the negative effect of heterogeneity, the ratio between  $D_{c20\%}$  and  $15^\circ$  mean unit size was added in the equation.

Based on Equation (1) [34] which was developed for ferritic-pearlitic and bainitic microstructures, a modified relationship was worked out for predicting the impact transition temperature in medium carbon ultrahigh-strength steels with tempered martensitic microstructure (Equation (3)). This modified approach included contributions by dislocation hardening,  $\sigma_p$ , and unaccounted strength,  $\sigma_{us}$ . Moreover, in this equation, the harmful effect of carbides was also considered. Following the approach by Mintz et al. [29], an additional term considering the impact of carbide size,  $t$ , was introduced.

$$\begin{aligned} \text{ITT50\%} = & -11(\% \text{Mn}) + 42(\% \text{Si}) + 700(\% \text{N}_{\text{free}})^{0.5} + 15(\% \text{MA})^{1/3} + 18(D_{\text{MA}})^{0.5} - 14(D_{15^\circ})^{-0.5} \\ & + 0.26(\sigma_p + \sigma_{us}) + 63 \left( \frac{D_{20\%}}{D_{15^\circ}} \right)^{0.5} + 112(t)^{0.5} \end{aligned} \quad (3)$$

Predicted ITT50% values based on Equation (3) are compared to experimental ones in Figure 11 for all alloys. The excellent agreement suggests that the modified relationship not only is appropriate for predicting transition temperatures of tempered martensitic microstructures but also allows for the identification of major influencing effects.

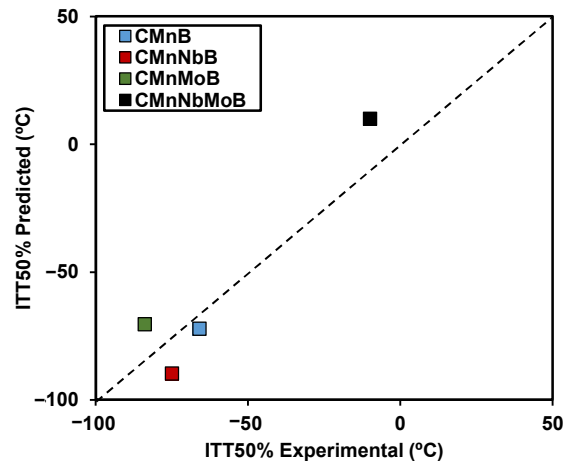


**Figure 11.** Correlation between predicted ITT50% considering Equation (3) and the experimental ITT50% measured by Charpy tests.

#### 3.4. Comparative Evaluation of Strengthening versus Transition Temperature

With the aid of Equation (3), the individual effects on the transition temperature in the current four alloy design can be analysed. Using the data for the various strengthening mechanisms in these alloys reported in a recent paper [35], vector diagrams have been constructed (Figure 12) according to the procedure proposed by Gladman [52]. Since the base composition for all four alloys is identical, the first three terms in Equation (3) do not account for any of the observed differences. Nitrogen is mostly bound into TiN particles in these alloys to protect boron. Hence, nitrogen is not expected to make a contribution to ITT50%. The contributions by Mn and Si lead to a strength increase by around 115 MPa without changing the transition temperature.

The MA phase was identified to be present in CMnNbB steel only. Its contribution to strength is marginal, but it does increase the ITT50%. Due to decomposition of the MA phase by tempering, it is expected to act similarly to the other temper carbides located at high- and low-angle boundaries, thus increasing the transition temperature.

The clearly biggest contribution to strength originates from microstructural refinement according to the Hall–Petch relationship. The generally extremely fine-grained structure of martensite in the current steels accounts for a yield strength increase of 450–520 MPa correlating in that range with the severity of austenite conditioning (Table 3) [6]. Simultaneously, the transition temperature significantly decreases with the strength increase, manifesting this well-established and unique benefit of microstructural refinement.

Other mechanisms such as dislocation strengthening and precipitation strengthening (denoted as unaccounted strength) cause an increase in transition temperature, which however is largely overcompensated by the microstructural refinement. Thus, the strategy for strengthening of first maximizing grain refinement before employing other mechanisms typically results in an improved ductile-to-brittle transition behaviour.

The main deleterious effect on the ductile-to-brittle behaviour in current steels is related to the heterogeneity in grain size distribution. Especially, the 20% fraction of largest grains is harmful to ITT50%, whereas its impact on strength is neutral. Large grains are more sensitive to cleavage at higher temperature than smaller ones. Simultaneously, the starting cracks caused by cleaving of larger individual grains are more likely to propagate. The fraction of very small prior austenite grains in the CMnNbB steel resulting from dynamic recrystallization is thus not expected to negatively affect ITT50%. However, the coexistence of very fine and larger grains can cause a serious level of residual stress in quenched steels, leading to macroscopic distortion [53]. The occurrence of very fine grains by dynamic recrystallization was found to be suppressed in current steels by sufficient

alloying of molybdenum. This Mo-based effect has also been confirmed by other studies [39].

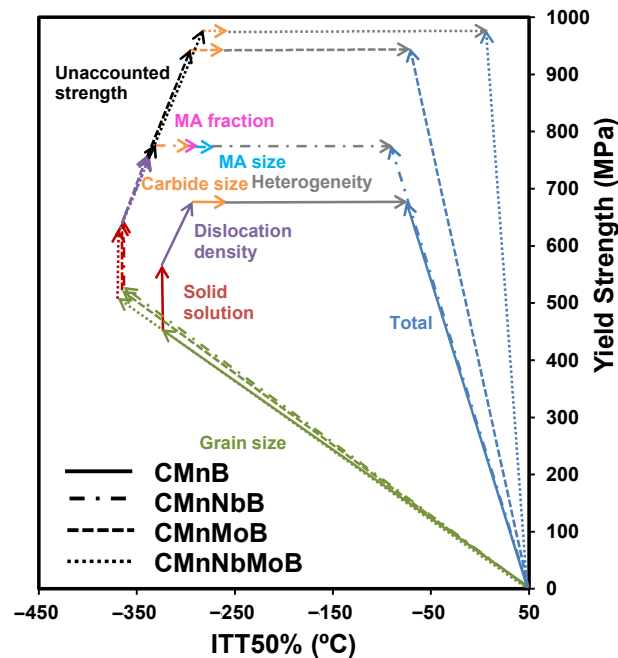


**Figure 12.** Relative contribution of different strengthening mechanisms (grain size, solid solution, dislocation density, unaccounted strength, presence of MA and heterogeneity) on both strength and toughness properties.

#### 4. Conclusions

It was demonstrated in the current study that steel having a yield strength of over 900 MPa and appreciably low ductile-to-brittle transition temperature (ITT50%) can be produced by direct quenching from the rolling heat followed by short tempering treatment (600 °C for 300 s). The use of molybdenum in a 0.15%CMnB base alloy is essential for reaching these targets.

The largest contribution to strength and toughness originates from martensite microstructural refinement. Significant refinement is inherent to the martensitic substructure. Additional refinement is related to austenite conditioning, which can be achieved by Nb microalloying (0.025%), Mo alloying (0.5%) or a combination of both.

The most harmful effect on ITT50% is related to microstructural heterogeneity and more particularly to the fraction of largest prior austenite grains. This heterogeneity was quantitatively determined from an EBSD-based austenite reconstruction procedure. The combined addition of Mo and Nb causes the most pronounced heterogeneity, which apparently is caused by incomplete recrystallization during the high-temperature deformation (roughing) stage. Optimizing the processing towards achieving a high degree of microstructural homogeneity therefore appears to be a more important target than solely focusing on maximum refinement.

Molybdenum was confirmed to suppress dynamic recrystallization occurring during austenite conditioning in the CMnB and the Nb-only alloyed steels. The very fine equiaxed austenite grains showed the tendency to transform into ferrite due to the absence of boron on the grain boundary. In that respect, molybdenum can be considered to have an indirect contribution to hardenability in addition to its well-known direct transformation-retarding effect.

**Author Contributions:** I.Z. carried out the experiments and wrote the manuscript; N.I. supervised the results, analysed the data and wrote the manuscript; E.D., V.S. and H.M. contributed to the interpretation of the data and edited the manuscript; P.U. managed the project and edited the manuscript. All authors have read and agreed to the published version of the manuscript.

**Funding:** This research received funding by the International Molybdenum Association (IMOA).

**Institutional Review Board Statement:** Not applicable.

**Informed Consent Statement:** Not applicable.

**Data Availability Statement:** Data sharing not applicable.

**Acknowledgments:** The authors would like to acknowledge the International Molybdenum Association (IMOA) for funding this project.

**Conflicts of Interest:** The authors declare no conflict of interest.

## References

1. Berns, H. On Toughness of Quenched and Tempered Steels, *Z. Werkstofftech* **1978**, *9*, 189–204, doi:10.1002/mawe.19780090605.
2. Mohrbacher, H. Property Optimization in As-Quenched Martensitic Steel by Molybdenum and Niobium Alloying. *Metals* **2018**, *8*, 234, doi:10.3390/met8040234.
3. Mohrbacher, H. Synergies of niobium and boron microalloying in molybdenum based bainitic and martensitic steel. *Fundam. Appl. Mo Nb Alloy. High Perform. Steels* **2014**, *1*, 83–108.
4. Larrañaga-Otegui, A.; Pereda, B.; Jorge-Badiola, D.; Gutierrez, I. Austenite Static Recrystallization Kinetics in Microalloyed B Steels. *Metall. Trans. A* **2016**, *47*, 3150–3164, doi:10.1007/s11661-016-3465z.
5. He, X.L.; Djahazi, M.; Jonas, J.J.; Jackman, J. The non-equilibrium segregation of boron during the recrystallization of Nb-treated HSLA steels. *Acta Met. Mater.* **1991**, *39*, 2295–2308, doi:10.1016/0956-7151(91)90012-P.
6. Hulka, K.; Kern, A.; Schrieffer, U. Application of Niobium in Quenched and Tempered High-Strength Steels. *Mater. Sci. Forum* **2005**, *500–501*, 519–526, doi:10.4028/www.scientific.net/MSF.500-501.519.
7. Sharma, M.; Ortlepp, I.; Bleck, W. Boron in Heat-Treatable Steels: A Review. *Steel Res. Int.* **2019**, *90*, 1900133, doi:10.1002/srin.201900133.
8. Revilla, C.; López, B.; Rodríguez-Ibabe, J.M. Carbide Size Refinement by Controlling the Heating Rate during Induction in a Low Alloy Steel. *Mater. Des.* **2014**, *62*, 296–304, doi:10.1016/j.matdes.2014.05.053.
9. Krauss, G. Martensite in steel: Strength and structure. *Mater. Sci. Eng. A* **1999**, *273*, 40–57, doi:10.1016/S0921-5093(99)00288-9.
10. Linaza, M.A.; Rodríguez-Ibabe, J.M.; Urcola, J.J. Determination of the energetic parameters controlling cleavage fracture initiation in steels. *Fatigue Fract. Eng. Mater. Struct.* **1997**, *20*, 619–632, doi:10.1111/j.1460-2695.1997.tb00296.x.
11. Maki, T.; Tsuzaki, K.; Tamura, I. The morphology of the strengthening of lath martensite in steels. *Trans. Iron Steel Inst. Jpn.* **1980**, *20*, 207–215, doi:10.2355/isijinternational1966.20.207.
12. Hannula, J.; Kömi, J.; Porter, D.A. Effect of boron on the strength and toughness of direct-quenched low-carbon niobium bearing ultra-high-strength martensitic steel. *Metall. Mat. Trans. A* **2017**, *48*, 5344–5356, doi:10.1007/s11661-017-4295-3.
13. Prawoto, Y.; Jasmawati, N.; Sumeru, K. Effect of prior austenite grain size on the morphology and mechanical properties of martensite in medium carbon steel. *J. Mater. Sci. Technol.* **2012**, *28*, 461–466, doi:10.1016/S1005-0302(12)60083-8.
14. Furuhashi, T.; Kikumoto, K.; Saito, H.; Sekine, T.; Ogata, T.; Morino, S. Phase transformation from fine-grained austenite. *ISIJ Int.* **2008**, *48*, 1038–1045, doi:10.2355/isijinternational.48.1038.
15. Khani Sanij, M.H.; Ghasemi Banadkouki, S.S.; Mashreghi, A.R.; Moshrefifar, M. The effect of single and double quenching and tempering heat treatments on the microstructure and mechanical properties of AISI 4140 steel. *Mater. Des.* **2012**, *42*, 339–346, doi:10.1016/j.matdes.2012.06.017.
16. Laasraoui, A.; Jonas, J.J. Recrystallization of Austenite after Deformation at High Temperatures and Strain Rates-Analysis and Modeling. *Metall. Trans. A* **1991**, *22*, 151–160, doi:10.1007/BF03350957.
17. Hutchinson, C.R.; Zurob, H.S.; Sinclair, C.W.; Brechet, Y.J.M. The comparative effectiveness of Nb solute and NbC precipitates at impeding grain-boundary motion in Nb steels. *Scripta Mater.* **2008**, *59*, 635–637, doi:10.1016/j.scriptamat.2008.05.036.
18. Isasti, N.; Jorge-Badiola, D.; Taheri, M.L.; Uranga, P. Microstructural and precipitation characterization in Nb-Mo microalloyed steels, estimation of the contributions to the strength. *Metals Materials Int.* **2014**, *20*, 807–817, doi:10.1007/s12540-014-5002-1.
19. Sanz, L.; López, B.; Pereda, B. Characterization of Austenite Microstructure from Quenched Martensite Using Conventional Metallographic Techniques and a Crystallographic Reconstruction Procedure. *Metals* **2018**, *8*, 294, doi:10.3390/met8050294.
20. Sanz, L.; Pereda, B.; López, B. Validation and Analysis of the Parameters for Reconstructing the Austenite Phase from Martensite Electron Backscatter Diffraction Data. *Metall. Mater. Trans. A* **2017**, *48*, 5258–5272, doi:10.1007/s11661-017-4289-1.
21. Germain, L.; Gey, N.; Mercier, R.; Blaineau, P.; Humbert, M. An advanced approach to reconstructing parent orientation maps in the case of approximate orientation relations: Application to steels. *Acta Mater.* **2012**, *60*, 4551–4562, doi:10.1016/j.actamat.2012.04.034.

22. Kaijalainen, A.; Pallaspuro, S.; Porter, D.A. Tempering of direct quenched low-alloy ultra-high-strength steel, Part I—Microstructure. *Adv. Mater. Res.* **2014**, *922*, 316–321, doi:10.4028/www.scientific.net/AMR.922.316.
23. Pallaspuro, S.; Kaijalainen, A.; Linnell, T.; Porter, D. Tempering of Direct Quenched Low-Alloy Ultra-High-Strength Steel, Part II—Mechanical Properties. *Adv. Mater. Res.* **2014**, *922*, 580–585, doi:10.4028/www.scientific.net/AMR.922.580.
24. Saastamoinen, A.; Kaijalainen, A.; Porter, D.; Suikkanen, P.; Yang, J.-R.; Tsai, Y.-T. The effect of finish rolling temperature and tempering on the microstructure, mechanical properties and dislocation density of direct-quenched steel. *Mater. Charact.* **2018**, *139*, 1–10, doi:10.1016/j.matchar.2018.02.026.
25. Hannula, J.; Kaijalainen, A.; Porter, D.; Somani, M.; Kömi, J. Evaluation of Mechanical Properties and Microstructures of Direct-Quenched and Direct Quenched and Tempered Microalloyed Ultrahigh-Strength Steels. *Steel Res. Int.* **2020**, 2000451, doi:10.1002/srin.202000451.
26. Isasti, N.; Badiola, D.J.; Taheri, M.L.; Uranga, P. Microstructural features controlling mechanical properties in Nb-Mo microalloyed steels. Part II: Impact toughness. *Metall. Mater. Trans. A* **2014**, *45*, 4972–4982, doi:10.1007/s11661-014-2451-6.
27. Irvine, K.J.; Pickering, F.B.; Gladman, T. Grain-refined C-Mn steels. *J. Iron Steel Inst.* **1967**, *205*, 161–182.
28. Mintz, B.; Peterson, G.; Nassar, A. Structure-property relationships in ferrite-pearlite steels. *Ironmak. Steelmak.* **1994**, *21*, 215–222.
29. Mintz, B.; Morrison, W.B.; Jones, A. Influence of carbide thickness on impact transition temperature of ferritic steels. *Met. Technol.* **1979**, *6*, 252–260, doi:10.1179/030716979803276246.
30. Gutierrez, I. Effect of microstructure on the impact toughness of Nb-microalloyed steel: Generalisation of existing relations from ferrite-pearlite to high strength microstructures. *Mater. Sci. Eng. A* **2013**, *571*, 57–67, doi:10.1016/j.msea.2013.02.006.
31. Pickering, F.B.; Gladman, T. Metallurgical Developments in Carbon Steels. *ISI Spec. Rep.* **1963**, *81*, 42.
32. From, A.; Sandstrom, R. Influence of mixed grain size distributions on the toughness in high and extra high strength steels. *Mater. Charact.* **1999**, *42*, 111–122 doi:10.1016/S1044-5803(98)00051-5.
33. Hanamura, T.; Yin, F.; Nagai, K. Ductile-brittle transition temperature of ultrafine ferrite/cementite microstructure in a low carbon steel controlled by effective grain size. *ISIJ Int.* **2004**, *44*, 610–617, doi:10.2355/isijinternational.44.610.
34. Larzabal, G.; Isasti, N.; Rodríguez-Ibabe, J.M.; Uranga, P. Evaluating Strengthening and Impact Toughness Mechanisms for Ferritic and Bainitic Microstructures in Nb, Nb-Mo and Ti-Mo Microalloyed Steels. *Metals* **2017**, *7*, 65, doi:10.3390/met7020065.
35. Zurutuza, I.; Isasti, N.; Detemple, E.; Schwinn, V.; Mohrbacher, H.; Uranga, P. Effect of Nb and Mo Additions in the Microstructure/Tensile Property Relationship in High Strength Quenched and Quenched and Tempered Boron Steels. *Metals* **2021**, *11*, 29, doi:10.3390/met11010029.
36. Uranga, P.; Gutierrez, I.; Lopez, B. Determination of recrystallization kinetics from plane strain compression tests. *Mater. Sci. Eng. A* **2013**, *578*, 174–180, doi:10.1016/j.msea.2013.04.077.
37. Wallin, K. *Modified Tank Fitting Algorithm Charpy Impact Data*; Research Seminar on Economical and Safe Application of Modern Steels for Pressure Vessels: Aachen, Germany, 2003.
38. Schambron, T.; Dehghan-Manshadi, A.; Chen, L.; Gooch, T.; Killmore, C.; Pereloma, E. Effect of Mo on Dynamic Recrystallization and Microstructure Development of Microalloyed Steels. *Met. Mater. Int.* **2017**, *23*, 778–787, doi:10.1007/s12540-017-6636-6.
39. Pereda, B.; Fernández, A.I.; López, B.; Rodríguez-Ibabe, J.M. Effect of Mo on Dynamic recrystallization behavior of Nb-Mo microalloyed steels. *ISIJ Int.* **2007**, *47*, 860–868, doi:10.2355/isijinternational.47.860.
40. Medina, S.F.; Hernandez, C.A. General expression of the Zener-Hollomon parameter as a function of the chemical composition of low alloy and microalloyed steels. *Acta Mater.* **1996**, *44*, 137–148, doi:10.1016/1359-6454(95)00151-0.
41. Lee, W.B.; Hong, S.G.; Park, C.G.; Park, S.H. Carbide precipitation and high-temperature strength of hot-rolled high strength, low alloy steels containing Nb and Mo. *Metall. Mater. Trans. A* **2002**, *33*, 1689–1698, doi:10.1007/s11661-002-0178-2.
42. Mejia, I.; Salas-Reyes, A.E.; Bedolla-Jacuinde, A.; Calvo, J.; Cabrera, J.M. Effect of Nb and Mo on the hot ductility behavior of a high-manganese austenitic Fe-21Mn-1.3Al-1.5Si-0.5C TWIP steel. *Mat. Sci. Eng. A* **2014**, *616*, 229, doi:10.1016/j.msea.2014.08.030.
43. Larzabal, G.; Isasti, N.; Rodríguez-Ibabe, J.M.; Uranga, P. Effect of Microstructure on Post-Rolling Induction Treatment in a Low C Ti-Mo Microalloyed Steel. *Metals* **2018**, *8*, 694, doi:10.3390/met8090694.
44. Calcagnotto, M.; Ponge, D.; Demir, E.; Raabe, D. Orientation gradients and geometrically necessary dislocations in ultrafine grained dual-phase steels studied by 2D and 3D EBSD. *Mater. Sci. Eng. A* **2010**, *257*, 2738–2746, doi:10.1016/j.msea.2010.01.004.
45. Uranga, P.; Shang, C.-J.; Senuma, T.; Yang, J.-R.; Guo, A.-M.; Mohrbacher, H. Molybdenum alloying in high-performance flat-rolled steel grades. *Adv. Manuf.* **2020**, *8*, 15–34, doi:10.1007/s40436-019-00285-y.
46. Djahazi, M.; He, X.L.; Jonas, J.J.; Sun, W.P. Nb(C, N) Precipitation and Austenite Recrystallization in Boron-Containing High-Strength Low-Alloy Steels. *Metall. Mater. Trans. A* **1992**, *23*, 2111–2120, doi:10.1007/BF02646004.
47. Mohrbacher, H. Mo and Nb alloying in plate steels for high-performance applications. Proc. International Symposium on the Recent Developments in Plate Steels. *Int. Symp. Recent Dev. Plate Steels* **2011**, 169–179. Available online: [https://www.researchgate.net/profile/Hardy\\_Mohrbacher/publication/333661101\\_Mo\\_and\\_Nb\\_Alloying\\_in\\_Plate\\_Steels\\_for\\_High-Performance\\_Applications/links/5cfb6da24585157d159b1ad7/Mo-and-Nb-Alloying-in-Plate-Steels-for-High-Performance-Applications.pdf](https://www.researchgate.net/profile/Hardy_Mohrbacher/publication/333661101_Mo_and_Nb_Alloying_in_Plate_Steels_for_High-Performance_Applications/links/5cfb6da24585157d159b1ad7/Mo-and-Nb-Alloying-in-Plate-Steels-for-High-Performance-Applications.pdf) access on 30 December 2020)
48. Kim, Y.M.; Shin, S.Y.; Lee, H.; Hwang, B.; Lee, S.; Kim, N.J. Effects of molybdenum and vanadium addition on tensile and charpy impact properties of API X70 linepipe steels. *Metall. Mater. Trans. A* **2007**, *38*, 1731–1742, doi:10.1007/s11661-007-9197-3.
49. Mohseni, P.; Solberg, J.K.; Karlsen, M.; Akselsen, O.M.; Østby, E. Cleavage fracture initiation at M-A constituents in intercritically coarse-grained heat-affected zone of a HSLA steel. *Metall. Mater. Trans. A* **2014**, *45*, 384–394, doi:10.1007/s11661-013-2110-3.

50. LePera, F.S. Improved etching technique for the determination of percent martensite in high-strength dual-phase steels. *Metallography* **1979**, *12*, 263–268, doi:10.1016/0026-0800(79)90041-7.
51. Pickering, F.B. The optimization of microstructures in steel and their relationship to mechanical properties. In *Hardenability Concepts with Applications to Steel*; Doane, D.V., Kirkaldy, J.S., Eds.; AIME: New York, NY, USA, 1978; pp. 179–228.
52. Gladman, T. *The Physical Metallurgy of Microalloyed Steels*, 2nd ed.; The Institute of Materials: London, UK, 1997; pp. 62–68.
53. Tobie, T.; Hippenstiel, F.; Mohrbacher, H. Optimizing Gear Performance by Alloy Modification of Carburizing Steels. *Metals* **2017**, *7*, 415, doi:10.3390/met7100415.